First results from the VSA - III. The CMB power spectrum

Paul F. Scott¹, Pedro Carreira², Kieran Cleary², Rod D. Davies², Richard J. Davis², Clive Dickinson², Keith Grainge¹, Carlos M. Gutiérrez³, Michael P. Hobson¹,

Michael E. Jones¹, Rüdiger Kneissl¹, Anthony Lasenby¹, Klaus Maisinger¹,

Guy G. Pooley¹, Rafael Rebolo^{3,4}, José Alberto Rubiño-Martin³, Pedro Sosa Molina³, Ben Rusholme^{1,*}, Richard D.E. Saunders¹, Richard Savage¹, Anže Slosar¹,

Angela C. Taylor¹, David Titterington¹, Elizabeth Waldram¹,

Robert A. Watson^{2,†}, Althea Wilkinson²

- ¹ Astrophysics Group, Cavendish Laboratory, University of Cambridge, UK
- 2 University of Manchester, Jodrell Bank Observatory, UK
- ³ Instituto de Astrofísica de Canarias, 38200 La Laguna, Tenerife, Spain.
- ⁴ Consejo Superior de Investigaciones Científicas, Spain
- *Present address: Stanford University, Palo Alto, CA, USA
- [†]Present address: Instituto de Astrofísica de Canarias.

2 December 2024

ABSTRACT

We present the power spectrum of the fluctuations in the cosmic microwave background detected by the Very Small Array (VSA) in its first season of observations in its compact configuration. We find clear detections of first and second acoustic peaks at $\ell \approx 200$ and $\ell \approx 550$, plus detection of power on scales up to $\ell = 800$. The VSA power spectrum is in very good agreement with the results of the BOOMERANG, DASI and MAXIMA telescopes despite the differing potential systematic errors.

Key words: cosmology:observations – cosmic microwave background

1 INTRODUCTION

Anisotropies in the Cosmic Microwave Background (CMB) have now been detected by many experiments (most recently Netterfield et al. (2001), Lee et al. (2001), Halverson et al. (2002), Padin et al. (2001)). At present the most successful model for explaining the origin of these fluctuations postulates that they are seeded in the very early universe by quantum perturbations with random phase, followed by a period of inflationary expansion. The fluctuations in the CMB are predicted to be Gaussian in nature, and hence can be completely characterised through their power spectrum. A further prediction is that the power spectrum will show acoustic peaks due to plasma oscillations on scales smaller than the sound horizon at the surface of last scattering.

In this paper we present the power spectrum of the CMB fluctuations detected by the Very Small Array (VSA) on spherical harmonic modes $\ell \approx 150$ –900. We outline how the fully calibrated time-stream data are converted into a power spectrum and the various data checks that we have performed to confirm the validity of our analysis. This paper is the third in a series of four papers which report the

results of the first season of observations made using the VSA in its compact configuration. Paper I (Watson et al. 2002) describes the design of the VSA and our experimental method; the observational strategy, foreground removal and reduction techniques for the data analysed in this paper are described in Paper II (Taylor et al. 2002); finally, the cosmological implications of the VSA power spectrum are discussed in Rubiño-Martin et al. (2002) (Paper IV).

2 OBSERVATIONS AND INITIAL DATA PROCESSING

2.1 The observations

The Very Small Array (VSA) is a 14-element interferometer array for Cosmic Microwave Background (CMB) observations; it operates at a frequency between 26 and 36 GHz with a receiver bandwidth of 1.5 GHz. In its compact configuration, used here, the instrument is most sensitive to angular structure in the range $\ell \approx 150-900$. As well as the 14-element array, there is also a single baseline interferometer used for

radio source flux measurements. A fuller description of the instrument is given in Paper I.

The present observations were made at a frequency of 34 GHz in the period 2000 September to 2001 September and were centred on three separate areas of sky. Each VSA observation maps a region with FWHM of 4.6° . The process of field selection is discussed in Paper II; selection was based primarily on low Galactic (synchrotron, free-free and dust) emission and an absence of known bright foreground sources. Overlapping fields were observed in each area in order to reduce the sample variance, to increase the resolution in ℓ -space and to allow for direct assessment of data reliability and the detection of any residual instrumental effects (Section 4.2). The array configuration used was designed to provide an approximately uniform spread of interferometer baselines while retaining a reasonable aperture filling factor.

The amplitude and phase calibrations of the individual interferometer baselines were checked both by frequent short measurements of a number of secondary calibration sources and also by regular longer observations of a small number of primary calibration sources. The overall calibration procedure is described fully in Paper I; the overall accuracy of the calibration in flux density and temperature is 3.5%.

An important aspect of the VSA is the inclusion of a separate interferometer, comprising two 3.7-m dishes on a 9-m north-south baseline, for determining the flux densities of foreground sources (radiogalaxies and quasars) falling within the observed fields. The positions of all sources which might affect the VSA observations were obtained from survey observations using the Ryle Telescope (Waldram et al. 2002); these positions were subsequently observed concurrently with the main VSA observations in a series of regular pointed observations (Paper II).

2.2 Initial Data Processing

The data are calibrated and processed as described in Papers I and II. Early tests of the telescope revealed an unwanted local spurious signal, particularly evident on the shorter baselines. The procedures for removing this signal from the data are described fully in Paper II; the tests presented in Section 4.2 below indicate that the removal of this signal is complete. Similar filtering processes were used to eliminate signals arising from the Sun and the Moon.

3 DERIVATION OF THE POWER SPECTRUM

Since the three sets of mosaiced fields are widely separated from one another on the sky, the data corresponding to each field are analysed individually. The derivation of the CMB power spectrum for each mosaic is performed using the maximum-likelihood method presented in Hobson & Maisinger (2002), which we summarise here. The results from each mosaic are then combined, as outlined below, to produce the final estimate of the power spectrum.

Since the number of individual visibility measurements for each mosaic is very large ($\sim 800,000$), it is first necessary to compress these data in some way. For each separate field in the mosaic, the visibilities are binned into cells in the uv-plane using a maximum-likelihood algorithm. This is analogous to the 'map-making' step in the analysis of

single-dish CMB observations, in which time-ordered data are binned into pixels on the sky (see, e.g. Borrill (1999)). Since we are not interested here in making accurate CMB maps from the binned visibility data, the uv-plane is simply divided into equal-area cells of size $\Delta u = 3$ wavelengths. As the aperture function of the compact VSA is well-modelled by a Gaussian with a FWHM of 12 wavelengths, this cell size ensures that the uv-plane is comfortably over-sampled, while reducing the total number of visibility measurements for each field significantly (to ~ 2500).

The binned visibilities are thus the basic input to the likelihood analysis for the CMB power spectrum. The compact VSA is sensitive to the multipole range $\ell \sim 150-900$, and the effective aperture function (after mosaicing) has a FWHM of $\Delta \ell = 83$. We thus divide the total ℓ -range into 10 (quasi-uncorrelated) spectral bands each of width $\Delta \ell$, in each of which we assume $\ell(\ell+1)C_{\ell}$ to have a constant value $\bar{\mathcal{C}}_B$ ($B=1,2,\ldots,10$). The assumed flat powers across each band are then the parameters to be determined in our likelihood analysis of the data for each mosaic. We denote these band powers collectively by the parameter vector \boldsymbol{a} .

Assuming the CMB emission and the instrumental noise to be Gaussian random fields, the log-likelihood of obtaining the binned visibility data vector \boldsymbol{v} (which contains the real and imaginary parts separately of each binned visibility), given some set of flat band powers \boldsymbol{a} , is given by

$$\ln \mathcal{L} = \text{constant} - \frac{1}{2} \left[\ln |C(a)| + v^{\text{t}} C^{-1}(a) v \right],$$

where C(a) = S(a) + N is the sum of the predicted signal covariance matrix and the noise covariance matrix. The maximum-likelihood CMB power spectrum \hat{a} is calculated using a simple iterative numerical maximisation algorithm. Starting from an initial guess a_0 (which is unimportant), independent line maximisations are performed for each band power C_B in turn, while keeping the others fixed. The whole solution vector a is then updated and the process repeated until convergence is obtained. This typically requires around 5 iterations.

The well-defined correlation structure of visibility data in the uv-plane allows each line-maximisation to be performed using only the subset of visibilities that are sensitive to the band power being varied, thereby speeding-up the evaluation of the likelihood function. For a single VSA mosaic, the maximum-likelihood solution can be obtained in around eight hours on an 8-node Beowulf Cluster with 1.8-GHz AMD Athlon processors.

The uncertainties in the derived maximum-likelihood CMB power spectrum are estimated in two complementary ways. Assuming the likelihood function in the parameter space a to be well-approximated by a multivariate Gaussian near its peak, the covariance matrix of the parameter uncertainties is given simply by (minus) the inverse of the curvature (or Hessian) matrix at the peak \hat{a} . This matrix is easily evaluated numerically in around half a day of CPU time. The square-root of the diagonal elements of the resulting covariance matrix give the standard error $\Delta \bar{C}_{\rm B}$ on each band power, whereas the off-diagonal elements provide a measure of the correlation between the band power estimates in different spectral bins. We find, typically, that adjacent bins are anti-correlated at around the 5–20% level, and for more widely separated bins the correlation is negligible.

Using the covariance matrix clearly produces symmet-

ric error bars on each band power $\bar{\mathcal{C}}_{\mathrm{B}}$, which may be a poor representation of the uncertainty, especially for poorly constrained band powers. An alternative approach is to make use of the fact that the band power estimates in different spectral bins are quasi-uncorrelated, so that the off-diagonal elements of the covariance matrix are small compared to those on the diagonal. In this case, a better representation of the uncertainty in each estimate may be obtained by directly evaluating the likelihood function through the peak \hat{a} , along each parameter direction in turn. In the ideal case, where the band power estimates are independent, the resulting curves would be the marginal distributions of each band power. Since the likelihood function can be evaluated very quickly along each direction in parameter space, the resulting 'marginal' distributions can be calculated for each VSA mosaic in around 2 hours, and provide a useful cross-check of the standard errors obtained from the covariance matrix at the peak.

Once the likelihood functions for the flat band power $\bar{\mathcal{C}}_B$ in each spectral bin have been obtained separately for each VSA mosaic, the mosaics are combined simply by multiplying together the respective likelihood functions in each bin. This assumes that each mosaic provides an independent measurement of the CMB power spectrum in each spectral bin, which is valid given that the three sets of mosaiced fields are widely separated on the sky. The correlation between the resulting band power estimates in different bins is easily obtained by calculating the covariance matrix, as described above, at the new joint optimum \hat{a} .

All the above functions are implemented using the MADCOW analysis package (Hobson & Maisinger 2002).

3.1 Window functions

Because of various instrumental effects (e.g. non-uniform uv coverage and the finite size of the primary beam of the telescope), a bin samples the underlying power spectrum C_l through a window function W(l). For the ith bin, the measured power corresponds to

$$p_i = \sum_{\ell} W_i(\ell) C_l(2\ell+1) / 4\pi.$$

The window function for a given bin is determined as follows. The Fourier modes to which a given visibility is sensitive are given by the aperture illumination function, which is the Fourier transform of the primary beam for a single field observations (see e.g. Hobson & Maisinger (2002)). For a Gaussian primary beam

$$\tilde{A}(\mathbf{u}) = 2\pi\sigma^2 \exp(-2\pi^2\sigma^2|\mathbf{u}|^2).$$

where \mathbf{u} is the vector in the visibility plane (measured in wavelengths). For mosaiced observations, the effective beam is a superposition of displaced primary beams. We can think of this superposition as a convolution of a centered primary beam with a sum of delta functions at the beam centres. In the Fourier domain this corresponds to a multiplication of the aperture function with the 'Fraunhofer diffraction pattern' of the beam centres

$$\tilde{A}_{\text{eff}}(\mathbf{u}) = \Sigma_j \tilde{A}(\mathbf{u}) e^{2\pi i \mathbf{u} \cdot \mathbf{x}_j},$$

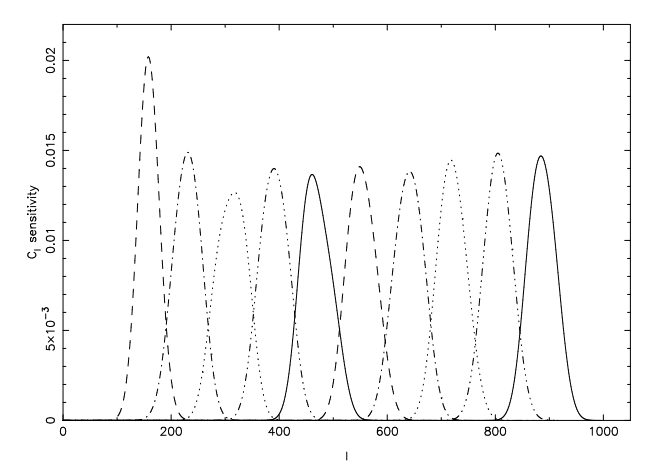


Figure 1. Window functions for the combined data set. The functions are normalised to unit area, and different bins are plotted with different linestyles to allow easier visual differentiation.

where \mathbf{x}_j are the positions of the beam centres from the origin, measured in radians. Note that in general this aperture function is complex.

For a given bin, the weighted complex sensitivity map is

$$S(\mathbf{u}) = \sum_{k} w_k \tilde{A}_{\text{eff}}(\mathbf{u} - \mathbf{v}_k),$$

where index k runs over visibilities in a given bin. These visibilities have instrumental weights w_k and positions on the visibility plane \mathbf{v}_k .

The un-normalised window function is then given by:

$$W(\ell) = \mathcal{N} \int_{\phi=0}^{\phi=2\pi} |S(\ell,\phi)|^2 \ell \,\mathrm{d}\phi,$$

where $\ell=2\pi|\mathbf{u}|$. The extra ℓ factor comes from the fact that $\mathrm{d}A=\ell\,\mathrm{d}\phi\mathrm{d}\ell$ and $\mathrm{d}\ell\approx\Delta\ell=1$. The normalisation constant $\mathcal N$ can be trivially found using $\sum_{\ell}(2\ell+1)W(\ell)/(2\ell(\ell+1))=1$. Figure 1 shows the VSA window functions for the combined data set.

4 DATA CHECKS

The complete process of editing and filtering the data and also the subsequent stages of data reduction were carried out independently by the Cambridge group and, jointly, by the combined IAC and JBO teams. A comparison of the two sets of results showed good agreement, the effect of any differences being small compared to the intrinsic uncertainties on the final power spectra.

4.1 Test of data reduction procedure

Aspects of our data reduction procedure, such as filtering and calibration, could potentially have introduced systematic errors into the VSA data. In order to test this, we produced a realisation of the CMB sky and simulated a mock VSA observation including such instrumental effects as visibility quadrature errors, phase steps due to path compensation and thermal noise. We analysed these simulated data using our standard reduction procedure and then produced

a power spectrum as described in section 3. We found this to be entirely consistent with our input model and so concluded that our method of data reduction did not introduce any significant systematic errors.

4.2 The Local Spurious Signal

The local spurious signal, fully discussed in Paper I, was found to depend only on the antenna tracking angle, and not on the table elevation. Therefore, we would expect the spurious signal to be identical for different fields with the same declination observed over the same hour angle range. This is easily confirmed by combining the (unfiltered) baseline timeseries of two such fields by both addition and subtraction. We find that adding the two fields enhances the spurious signal, whilst subtraction entirely removes it. Whilst this technique of addition and subtraction is adequate for detecting the presence of spurious signal in unfiltered data, it is insufficiently sensitive to detect possible low level residual signal once filtering has been applied.

The increase in detection sensitivity that we require in order to test the filtered data for residual spurious signal can, however, be obtained using a modified version of a MEM algorithm used for extraction of CMB signal from VSA data (Maisinger et al. 1997).

We add an extra term to the MEM reconstruction which is the signal that is identical in the CMB datasets. We then consider the case of two fields at identical declination. As the CMB signal in the two fields will not be identical, and the noise is random in each case separately, any common component to the two fields will be spurious signal.

We tested this algorithm by applying it to pairs of simulated observations of CMB fields assuming CDM primordial fluctuations, to which we added an identical component with an rms level such that it was not the dominant signal. We used a variety of common components, including a scaled down version of the unfiltered spurious signal. We found that the MEM algorithm was able to reconstruct the common signals well, recovering the structure excellently, and recovering the amplitude of the signal to within 10%. As we are primarily interested in whether or not the spurious signal is still present, as opposed to any accurate quantification, this is perfectly adequate. Note that, even for entirely independent fields, the reconstructed shared signal power spectra are not zero (Figure 2, upper plot), but rather show a value increasing as ℓ^2 . This is consistent with the correlation between two white noise signals.

The two VSA2 fields had identical declination to allow testing of our filtering procedures. The MEM algorithm was applied to these fields, and the results compared with CDM realisations with identical uv-coverage and thermal noise in which no shared signal is present. The results (Figure 2) show that the degree of common signal found from the real data fields and the simulations are identical within the errors. We conclude that there is no significant spurious signal remaining in the VSA2 fields. In the same manner, we find no evidence for residual spurious signal in the pairs of VSA1,3 fields at similar declination.

Non-Gaussianity analysis of the binned visibilities allows us to locate and remove the few remaining visibilities contaminated with spurious signals down to a low level. The removal of these points has a negligible effect on the final

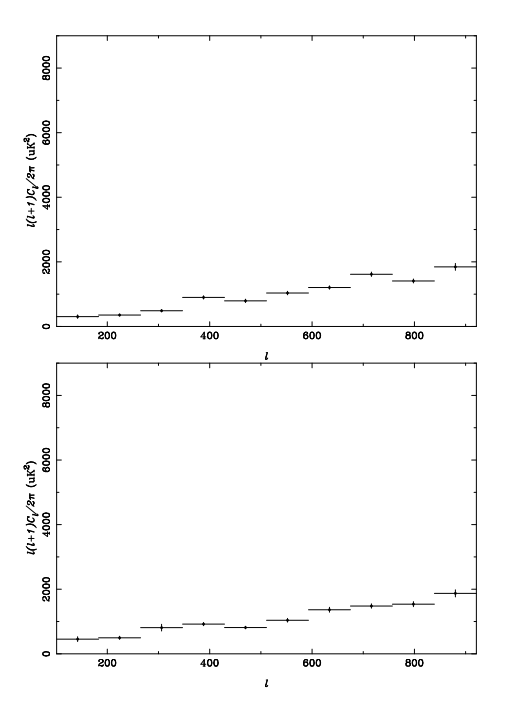


Figure 2. Power spectrum of the recovered common signal from: (upper plot) a pair of simulated datasets with no common signal (i.e. independent noise only); (lower plot) the two VSA2 fields. Coverage of the *uv*-plane and the thermal noise level are identical for both the simulation and the real data. The two plots are consistent with each other, indicating that there is no significant component of the spurious signal remaining in our data after filtering.

power spectrum, giving us confidence that we are subtracting the spurious signal to a level well below that which could affect our results. The full details of this analysis will be published in Savage et al. in prep.

4.3 Foreground Source Subtraction

Radio galaxies and quasars are a significant contaminant of the CMB at microwave frequencies and in the higher ℓ ranges will dominate the CMB signal, making it essential to remove their contribution. Tests with simulated fields have been used to assess the potential contribution, before subtraction, of these sources to the final CMB spectrum. We generated ten realisations of the CMB sky using a particular CDM model and added to these the sources that we have observed to be present in the VSA1 field. We have then compared the power spectra recovered from simulated VSA observations with and without sources. Two of these simulations, representing the range of results obtained from the ten simulations, are shown in Figure 3. It is apparent that, with the fairly small number of sources in any one VSA field (typically 12 sources), the impact on the power spectrum is unpredictable. Although the main contribution tends to be in the higher ℓ -bins (with errors potentially reaching $\pm 100\%$ at $\ell = 900$), changes of up to $\pm 10\%$ can occur in the lowest *l*-bin; these are due to the chance superposition of interference fringes.

To determine the effect of residual sources on the VSA results, two further simulations *without* a CMB contribution have been carried out. We base these simulations on the 15-

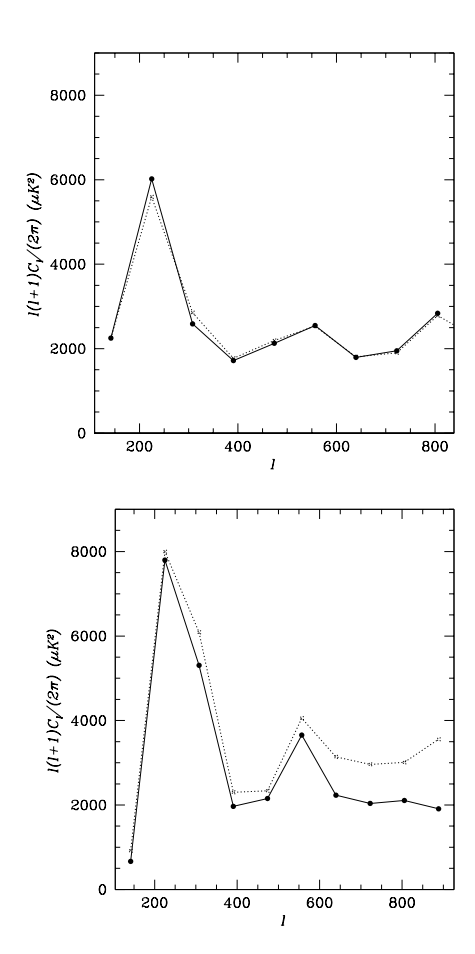


Figure 3. Two examples of recovered power spectra from simulated CMB observations with (filled circles, solid lines) and without (open circles, dotted lines) the known sources in the VSA1 field added. The differences arise from chance interactions between the sources and individual CMB features.

GHz source counts from Taylor et al. (2001) and extrapolate up to 34 GHz using a mean spectral index of $\alpha = 0.55$. The first (Figure 4 upper plot) comprises the contributions of the known point sources and a statistical distribution of weaker sources; the second (lower plot) includes only the statistical contribution of weaker sources and gives an indication of the possible residual contribution to the VSA power spectrum after subtraction of known sources. It is clear that, with no source subtraction, the CMB data are significantly compromised for ℓ -values $\geqslant 600$. After subtraction of known sources, the contribution is reasonably small for ℓ -values up to about 1000. As demonstrated by the results of Figure 3, the contribution of sources to the observed spectra can not generally be predicted from a simple combination of simulated power spectra, although such an approach becomes feasible in the limiting case of many weak sources per synthesised beam.

We can also estimate the residual source contribution to the power spectrum using the preliminary 34 GHz source count derived from the source subtractor observations in Paper II. Integrating the count from zero flux to our complete source subtraction limit of 80 mJy and converting to units of $\Delta T/T_0$, the source power is given by $C_\ell = 7.7 \times 10^{-16}$, corresponding to a power spectrum value of $\frac{\ell(\ell+1)}{2\pi}C_\ell T_0^2 =$

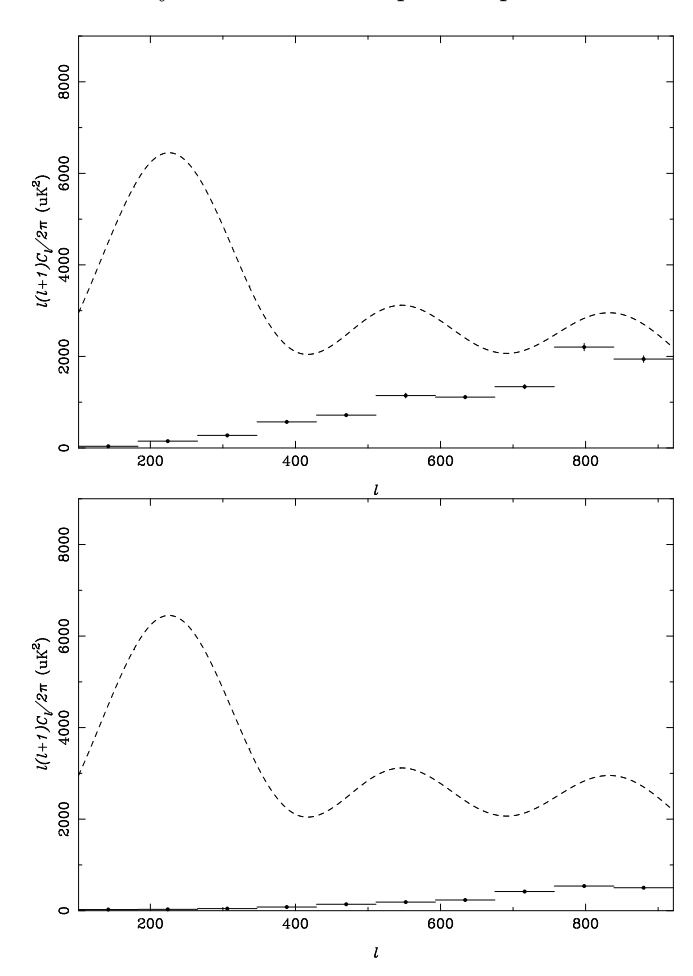


Figure 4. Simulated power spectra for known sources plus a statistical distribution of weaker sources (upper plot) and for the distribution of weaker sources alone (lower plot). For comparison the dashed curve shows the predicted power spectrum for a CDM model.

 $900\,\mu\mathrm{K}^2$ at $\ell=1000$. For the case with effectively no source subtraction, taking the upper flux limit to be 0.5 Jy, we find $C_\ell=3.7\times10^{-15}$, equivalent to $4100\,\mu\mathrm{K}^2$ at $\ell=1000$. These results are in excellent agreement with the extrapolations from the 15 GHz counts, and we estimate that residual uncertainties due to foreground sources, after subtraction, are less than 2.5 percent for ℓ -bins $\leqslant 800$.

4.4 Galactic Foregrounds

The diffuse Galactic foregrounds have been discussed in Paper II; here we discuss their effect on the results presented in this paper. We have shown that the total contribution from the three components of the Galactic foreground (synchrotron, free-free and possibly spinning dust) amount to no more than about $\Delta T = 5~\mu {\rm K}$ at an angular scale of 1° ($\ell \sim 200$). The free-free and synchrotron components are relatively well-known and are each expected to contribute about $\Delta T = 1 - 2~\mu {\rm K}$. The spinning dust component is more uncertain, but may be the dominant component, perhaps contributing up to $\Delta T \approx 5~\mu {\rm K}$. This is based on a dust-correlated component with a correlation coefficient of $10~\mu {\rm K}/({\rm MJy~sr}^{-1})$ at $100~\mu {\rm m}$. This coefficient is still to be clearly demonstrated observationally. The power spectra of

the diffuse foregrounds falls with increasing ℓ (for example, Giardino et al. (2001), Dickenson et al. in prep.) and is likely to be half these values at $\ell \sim 500$.

Any Galactic contribution adds in quadrature with the CMB power spectrum and hence at the position of the first CMB peak ($\ell \sim 200$) which has $\Delta T_{\rm CMB} \approx 75 \ \mu {\rm K}, 5 \ \mu {\rm K}$ of foreground signal will increase the observed signal by $0.17 \ \mu \text{K}$. Similarly, at $\ell \sim 500 \ \text{where} \ \Delta T_{\text{CMB}} \approx 45 \ \mu \text{K}$, the increase will be 0.28 μ K at the most. We see therefore, for the VSA fields, and at a frequency of 34 GHz, that Galactic foregrounds are negligible. A more complete cross-correlation analysis to investigate the contribution from dust-correlated emission is in progress (Dickinson et al. 2002).

Noise Estimation 4.5

The likelihood analysis used for power-spectrum estimation requires an accurate estimate of the rms noise level. Since on individual baselines the contribution of the CMB to the individual data samples is very small, the noise level can be obtained directly from the standard deviation of the data, after the filtering and flagging processes have been completed. The noise level associated with each of the binned visibilities (Section 3) is obtained from an appropriately weighted combination of the noise levels of the data in each bin. As an additional check, the scatter in the data points contributing to each bin has also been used to provide a noise estimate. Consistent estimates of the noise level were obtained by the two methods. The overall noise estimate is accurate to 2.5%.

The sensitivity of the likelihood analysis to errors in the noise level has been tested by analysing the same dataset with different assumed levels of noise; the corresponding changes in estimated CMB power are less than 1% for ℓ values up to ~ 750 .

4.6Data Splits

As an additional check on the consistency of the data, we repeated our power spectrum analysis splitting our data set according to the following criteria:

- (i) Data split according to observing season.
- (ii) Data split into two with alternate visibilities in the time stream.
 - (iii) Data split into night/day observations.
 - (iv) Data split into individual field mosaics.

We found in all cases that power spectra from the split data sets were consistent with the estimated errors.

THE POWER SPECTRUM

The filtered and source-subtracted data for each of the VSA fields have been analysed using the MADCOW software package (Hobson & Maisinger 2002) as described in Section 3. The combination of the three mosaiced spectra is shown in Figure 5. The bin width used is $\Delta \ell = 83$, which gives quasiindependent errors in each bin. The actual correlations between bins are given by the correlation matrix (Table 2). To reduce the bias in assessing features in the power spectrum caused by the settings of the bin centres, we have also calculated the power spectrum with bin centres shifted by

B	ℓ	$\ell(\ell+1)C_{\ell}/2\pi[\mu\mathrm{K}^2]$		
1	142	3953^{+1709}_{-1248}		
1A	184		5246^{+1493}_{-1211}	
2	224	6200^{+1382}_{-1122}		
2A	266		6494^{+1233}_{-1040}	
3	307	3496^{+713}_{-661}		
3A	349		2080^{+460}_{-416}	
4	390	2122^{+416}_{-416}		
4A	432		1954^{+497}_{-371}	
5	473	1498^{+497}_{-460}		
5A	515		2452^{+624}_{-535}	
6	556	3246^{+787}_{-705}		
6A	598		1998^{+750}_{-705}	
7	639	1207^{+795}_{-662}		
7A	681		2162^{+876}_{-787}	
8	722	2039^{+1003}_{-869}		
8A	764		666_{-665}^{+917}	
9	806	499^{+1292}_{-499}		
9A	847		1954^{+1664}_{-1413}	
10	888	1914^{+1873}_{-1543}		
10A	930		541^{+2832}_{-541}	

Table 1. The power spectrum from combining the three VSA fields. The two sets of bin numbers (1, 1A etc) refer to the main and alternate binnings, the latter being shifted by half a bin width. All the bins have $\Delta \ell = 83$. The reported errorbars correspond to 68% confidence limits and were calculated by enclosing 68% area under a likelihood curve assuming independent bins. For further data analysis it is neccessary to use full window functions and covariance matrices that can be downloaded from our website. In addition to these errors, there is an overall 7% calibration uncertainty in power.

В	$\mathcal{C}_{B,B-2}$	$\mathcal{C}_{B,B-1}$	$\mathcal{C}_{B,B}$	$C_{B,B+1}$	$\mathcal{C}_{B,B+2}$	$Cov_{B,B}$
1			1.00	-0.06	0.00	18.78
2		-0.06	1.00	-0.13	0.00	15.53
3	0.00	-0.13	1.00	-0.07	0.02	4.86
4	0.00	-0.07	1.00	-0.18	0.06	1.98
5	0.02	-0.18	1.00	-0.18	0.01	2.46
6	0.06	-0.18	1.00	-0.15	0.05	6.19
7	0.01	-0.15	1.00	-0.22	0.02	5.96
8	0.05	-0.22	1.00	-0.16	0.03	10.06
9	0.02	-0.16	1.00	-0.21		12.41
10	0.03	-0.21	1.00			35.88

Table 2. The correlation matrix $C_{i,j}$ for the combined VSA data set (main binning only). These are calculated by normalising the covariance matrix of errors. Note that the correlation is only significant for adjacent bins. The values of matrix for which $C_{i,j}$ is not reported can be assumed to be zero. The final column gives the diagonal elements of the covariance matrix in units of $10^5 \times \mu \mathrm{K}^4$

one half a bin width to the right of the original bin centres. These results are shown in Figure 5 with dashed error bars. Adjacent 'double-binned' points are highly correlated but do sensibly sample the power spectrum of our data. Numerical values for both binnings are given in Table 1.

The plotted error bars contain the contributions from both thermal noise and sample variance, but not calibration errors, which introduce a completely correlated uncertainty in all the points of ± 7 percent. Errors from pointing and primary beam uncertainties are negligible. Since the temperature sensitivity of the VSA compact configuration falls off dramatically after $\ell=800$, all data above this have been binned together.

6 DISCUSSION

6.1 The VSA power spectrum

The power spectrum shown in Figure 5 shows a clear detection of the first peak at $\ell \simeq 220$, and power at the level of about $2000 \,\mu\text{K}^2$ between $\ell = 300$ and $\ell = 900$. We have attempted to quantify the detection of a second peak at $\ell \simeq 550$, as this is the region of the power spectrum with the largest anti-correlations between adjacent bins (see Table 2); bin 6 centred at $\ell = 556$ is anti-correlated with its neighbours at the $\simeq 20$ percent level. We made Monte Carlo simulations of the five C_{ℓ} points between $\ell = 390$ and $\ell = 722$. Points were draw from the 5-dimensional gaussian distribution described by the actual correlation matrix of these points, but with mean values equal to the weighted mean of the five actual points. Following Hobson & Magueijo (1996) we then calculated the normalised convexity of the spectrum about the inner 3 points, defined by

$$\Sigma_i = \frac{|\langle \mathcal{C}_i \rangle|}{\sigma(\mathcal{C}_i)},$$

where $C_i = (C_{i-1} + C_{i+1})/2 - C_i$ and $\sigma^2(C_i)$ is the overall error in C_i .

In 100 realisations, we found only one instance of a convexity as large as the one observed in the real data about the $\ell=556$ point. We therefore conclude that the observed second peak is detected at 99 percent confidence. The power spectrum is completely consistent with the adiabatic inflationary models, fits to which are discussed in Paper IV.

6.2 Comparison with other experiments

In Figure 6 we compare the new VSA power spectrum plotted with those from BOOMERANG (Netterfield et al. 2001), DASI (Halverson et al. 2002), MAXIMA (Lee et al. 2001). Only single-binned (quasi-independent) points are shown. We have attempted to compare the random and correlated errors on the various experiments in a consistent way, difficult though this is on a single plot. Two sets of error bars are shown for each plot; the smaller bars indicate 68 percent confidence limits from the random (thermal and sample variance) errors, while the larger error bars represent systematic (calibration and beam) errors as reported – all the points from a single experiment are able to move up or down within the larger error bars.

The agreement between the experiments on the existence, heights and positions of two peaks and of power at higher ℓ , is evident. This is particularly significant given the very different experimental techniques involved and the different foregrounds and systematic errors faced by the different experiments. The points in Figure 6 have been obtained over a frequency range of 26–150 GHz, and by ground-based interferometers and balloon-borne scanned total-power telescopes. They are all from different regions of the sky, the calibrations are all independent and based on different absolute

calibration sources, and for the two low-frequency experiments foreground sources have been subtracted in different ways, yet the agreement of the power spectra is striking.

A detailed comparison between the experiments is difficult to do from the data points alone because of the correlated errors between points for each experiment. To make a meaningful comparison it is necessary to fit the underlying power spectrum to each data set, taking into account the correlations, and to compare the parameters that describe the power spectrum. In principle many parameterisations of the power spectrum would suffice for this comparison, but in practice it is obviously sensible to use the standard adiabatic cold dark matter power spectrum models, and fits to these models for the VSA and other experiments are considered in detail in Paper IV.

7 CONCLUSIONS

We have derived the power spectrum of the CMB anisotropies from the first year's VSA observations, made using its compact array configuration. We measure the flat band power in 10 quasi-independent bins of width $\Delta \ell = 83$ between $\ell \simeq 150$ and $\ell \simeq 900$. The results are subject to a calibration uncertainty of ± 7 percent in power, with negligible beam uncertainty. The contribution to the power spectrum from diffuse Galactic emission and residual radio sources is also negligible. Our results are in excellent agreement with other recent measurements as regards the amplitude and position of two peaks in the power spectrum; power is also detected out to the resolution limit of the experiment at $\ell \simeq 900$.

Band powers, correlation matrices and window functions are available from

http://mrao.cam.ac.uk/telescopes/vsa/results.html.

ACKNOWLEDGEMENTS

We thank the staff of the Mullard Radio Astronomy Observatory, Jodrell Bank Observatory and the Teide Observatory for invaluable assistance in the commissioning and operation of the VSA. The VSA is supported by PPARC and the IAC. Partial financial support was provided by Spanish Ministry of Science and Technology project AYA2001-1657. A. Taylor, R. Savage, B. Rusholme, C. Dickinson acknowledge support by PPARC studentships. K. Cleary and J. A. Rubiño-Martin acknowledge Marie Curie Fellowships of the European Community programme EARASTARGAL, "The Evolution of Stars and Galaxies", under contract HPMT-CT-2000-00132. K. Maisinger acknowledges support from an EU Marie Curie Fellowship. A. Slosar acknowledges the support of St. Johns College, Cambridge. We thank Professor Jasper Wall for assistance and advice throughout the project.

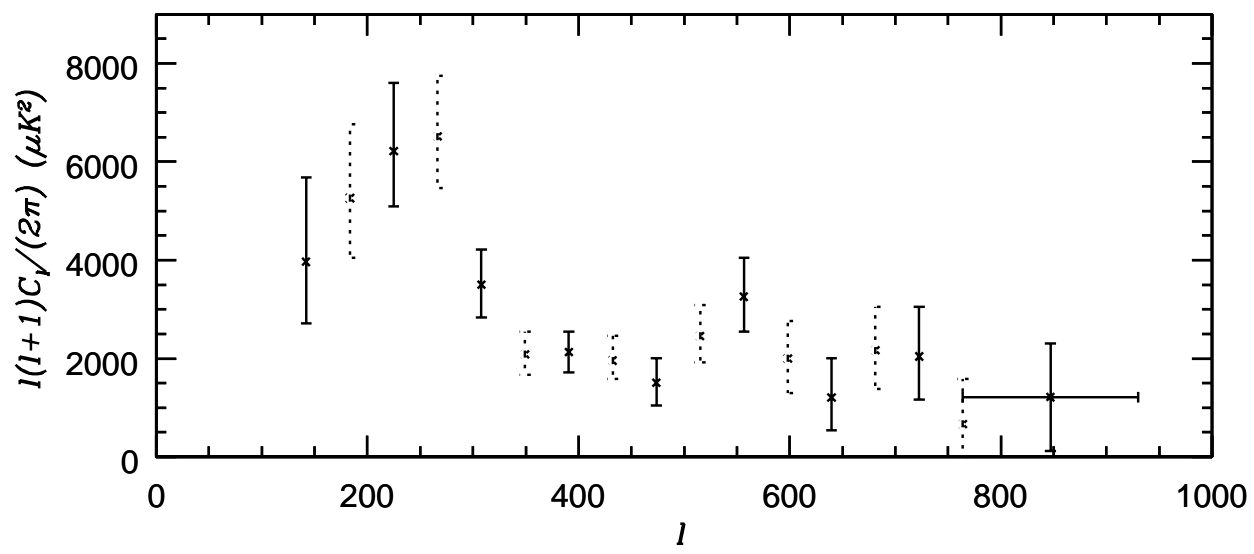


Figure 5. Combined CMB power spectrum from the three mosaiced VSA fields. The error-bars represent 1σ limits; the two sets of data points correspond to alternative interleaved binnings of the data.

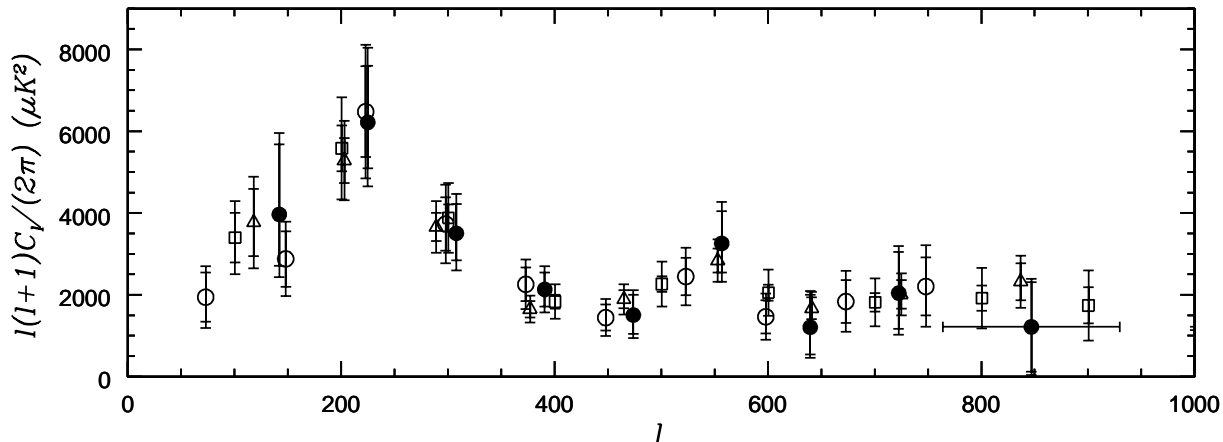


Figure 6. A comparison of the VSA data (filled circles) with results from the BOOMERANG (open squares), MAXIMA (open circles) and DASI (open triangles) experiments. Two sets of error bars are plotted for each data set; the smaller of the two indicate only random errors, whilst the larger bars indicate the amount by which the inner points could move due to absolute calibration and beam uncertainty. In each case the error bars indicate 1σ limits.

REFERENCES

- Borrill J., 1999, in AIP Conf. Proc. 476: 3K cosmology The Challenge of Data Analysis for Future CMB Observations. pp 277+
- Dickinson C., et al., 2002, The Power Spectrum of Diffuse Galactic Foregrounds, In preparation for submission to Mon. Not. R. Astron. Soc.
- Giardino G., Banday A. J., Fosalba P., Górski K. M., Jonas J. L., O'Mullane W., Tauber J., 2001, A&A, 371, 708
- Halverson N. W., et al., 2002, ApJ, 568, 38
- Hobson M. P., Magueijo J., 1996, MNRAS, 283, 1133
- Hobson M. P., Maisinger K., 2002, Maximum-likelihood estimation of the CMB power spectrum from interferometer observations, Accepted by Mon. Not. R. Astron. Soc., preprint astro-ph/0201438
- Lee A. T., et al., 2001, Astrophys.J., 561, L1
- Maisinger K., Hobson M. P., Lasenby A. N., 1997, MNRAS, 290, 313
- Netterfield C., et al., 2001, A measurement by BOOMERANG of multiple peaks in the angular power spectrum of the cosmic microwave background, Accepted by Astrophys.J., astro-ph/0104460
- Padin S., Cartwright J. K., Mason B. S., Pearson T. J., Readhead A. C. S., Shepherd M. C., Sievers J., Udomprasert P. S., Holzapfel W. L., Myers S. T., Carlstrom J. E., Leitch E. M., Joy M., Bronfman L., May J., 2001, Astrophys.J., 549, L1
- Rubiño-Martin J. A., et al., 2002, First results from the Very Small Array IV: Cosmological Parameter Estimation, Submitted to *Mon. Not. R. Astron. Soc.*
- Taylor A. C., et al., 2002, First results from the Very Small Array II: observations of the CMB, Submitted to Mon. Not. R. Astron. Soc.
- Taylor A. C., Grainge K., Jones M. E., Pooley G. G., Saunders R. D. E., Waldram E. M., 2001, MNRAS, 327, L1
- Waldram E. M., Pooley G. G., Grainge K. J. B., Jones M. E., Saunders R. D. E., Scott P. F., Taylor A. C., 2002, A Survey of Radio Sources at 15 GHz with the Ryle Telescope: Techniques and Properties, Submitted to *Mon. Not. R. Astron. Soc.*
- Watson R. A., et al., 2002, First results from the Very Small Array I: observational methods, Submitted to *Mon. Not. R. Astron. Soc.*

This paper has been type set from a TeX/ $\mbox{\sc IATeX}$ file prepared by the author.